Giant Modulation of Second-Harmonic Generation in $CuInP_2S_6$ by Interfacing with MoS_2 Atomic Layers

Dawei Li,[1,] Xinyi Hou,[1] Fanyi Kong,[1] Kun Wang,[2] and Xia Hong[2,*]*

[1] School of Optoelectronic Engineering and Instrumentation Science, Dalian University of Technology, Dalian, Liaoning 116024, China

[2] Department of Physics and Astronomy, University of Nebraska-Lincoln, Lincoln, NE 68588-0511, United States

* Address correspondence to: dwli@dlut.edu.cn, xia.hong@unl.edu

ABSTRACT: Probing and manipulating the intriguing nonlinear optical responses in van der Waals (vdW) ferroelectrics offer opportunities for their applications in nanophotonics. Here, we report the observation of giant and tunable second-harmonic generation (SHG) in ferroelectric $CuInP_2S_6$ (CIPS) and CIPS/MoS_2 heterostructures. The results show that CIPS, ranging from multi-layer to bulk-like samples, all exhibits strong SHG with giant anisotropy. The SHG anisotropy is attributed to the local strain along *a*-axis that naturally exists in CIPS, as evidenced by piezoresponse force microscopy measurement. We have further realized the strong modulation of SHG in CIPS by interfacing with monolayer MoS_2. A combination of polarization, temperature and thickness-dependent SHG and photoluminescence analyses shows that the nonlinear optical signal control in CIPS/MoS_2 heterostructures is unrelated to the polar symmetry of CIPS and MoS_2, but is driven by light absorption mediated interfacial coupling. Our study provides a material platform based on vdW ferroelectric heterostructures for achieving dynamic control of nonlinear optical responses, which shows great potential applications in modern nanophotonics.

KEYWORDS: *van der Waals ferroelectrics, $CuInP_2S_6$, second-harmonic generation, nonlinear light modulation, interfacial coupling, ferroelectric heterostructure*

INTRODUCTION

In recent years, two-dimensional (2D) van der Waals (vdW) ferroelectrics have attracted intensive research interest as they can retain robust ferroelectricity down to the monolayer limit and show great potential applications in nanoelectronics and optoelectronics.[1-3] Typical 2D ferroelectric materials include $CuInP_2S_6$ (CIPS) with out-of-plane polarization,[4] SnTe with in-plane polarization,[5] and α-In_2Se_3 with intercorrelated in-plane and out-of-plane polarization.[6] Among them, CIPS is one of the most stable 2D ferroelectrics, with the Curie temperature (T_C) above room temperature,[4, 7] which is critical for practical applications. It also exhibits many distinct physical properties, such as high ionic conductivity,[8] strong thermal anisotropy,[9] giant negative piezoelectricity and electrostriction,[10-11] inverse ferroelectric switching,[12] and high-efficiency catalysis.[13] CIPS can be further interfaced with other vdW materials into ferroelectric heterostructures, making them promising for multifunctional and reconfigurable device applications such as nonvolatile memories,[14-16] vdW negative capacitance transistors,[17] and ferroelectric diodes and tunnel junctions.[18-19] All of above applications are based on the ferroelectric and electrical characteristics of CIPS. However, the optical properties, especially the nonlinear optical responses of 2D ferroelectrics and ferroelectric heterostructures remain not well explored,[20] limiting their potential applications in modern nanophotonics, such as photovoltaics,[21] photodetectors,[22] optical filters,[23] quantum light sources,[24] ultrathin polarizers and waveplates.[25-26]

The optical second-harmonic generation (SHG) is one of the most important nonlinear optical phenomena in polar materials, which has been demonstrated in a wide range of 2D materials, from semiconducting layered transition metal chalcogenides (e.g., MoS_2, $MoSe_2$, GaSe, GaTe) to insulating *h*-BN.[27-31] The SHG emissions from these 2D materials are due to their broken inversion symmetry and large second-order nonlinear susceptibility, but the strong signal is only allowed in monolayer and few-layer samples owning to wave propagation and light absorption effects.[27-28] Strong SHG has also been experimentally discovered in 2D ferroelectrics with in-plane polarization[32]

or dipole locking.[33] However, the intrinsic property and modulation of nonlinear optical responses in out-of-plane dominated 2D ferroelectrics like CIPS have not been fully explored to date.[34-35]

In this study, we report the intrinsic optical SHG response in ferroelectric CIPS and giant modulation of SHG in CIPS by interfacing with transition metal dichalcogenide (TMDC) atomic layers. Experimental results show that the CIPS exhibits excellent SHG performance from few-layer to bulk-like dimension, which can be attributed to the broken inversion symmetry in all layer numbers. In addition, strong anisotropic SHG polarization patterns are observed in CIPS with different thicknesses, suggesting that a strain along the *a*-axis of CIPS naturally exist, as evidenced by piezoresponse force microscopy (PFM). By interfacing CIPS with monolayer (1L) MoS_2, we achieve strong modulation of SHG signals at the heterostructures. The tailored SHG signal at CIPS/1L-MoS_2 heterointerface is unrelated to the polar symmetry coupling, as evidenced by polarization-dependent SHG measurements, but can be attributed to the light absorption mediated interfacial coupling, as firmly confirmed by a combination of temperature and thickness-dependent photoluminescence (PL) and SHG analyses. Our study points to a materials strategy based on vdW ferroelectric heterostructures for designing photonic applications in nonlinear optics and nanophotonics.

RESULTS AND DISCUSSION

Giant and Anisotropic SHG Response in Ferroelectric CIPS. Few- to thick-layer CIPS flakes are mechanically exfoliated from bulk crystals and transferred onto the fused silica substrate. The topography and thickness of CIPS flakes are identified by optical imaging and atomic force microscopy (AFM). 2D CIPS belongs to monoclinic space group (*Cc*) at room temperature (Figure 1a).[36] To confirm its chemical structure, we have performed Raman analysis. Figure 1b shows the Raman spectrum of a thick-layer CIPS. Several active modes are observed, including the vibration peak for the cations (Cu^+ and In^{3+}) at 297.4 cm^{-1}, δ(S-P-P) mode at 157.4 cm^{-1}, δ(S-P-S) mode at 269.9 cm^{-1}, and ν(P-P) mode at 377.7 cm^{-1}, consistent with the previously reported ferroelectric CIPS structures.[37-38] We then use a homemade optical system to investigate the nonlinear optical responses

in CIPS. By introducing an 800 nm femtosecond (fs) laser beam ($\hat{e}_{\omega}$) as an excitation source and focusing onto the sample surfaces at normal incidence, an emission spectrum with strong peak at a wavelength of ~400 nm is detected (not shown), which is frequency doubled signal of the excitation laser. In addition, the emitted peak intensity follows a square power law behavior as a function of incident laser power (Figure 1c), further confirming the second-harmonic emission ($\hat{e}_{2\omega}$). The detected SHG signal from CIPS reveals its non-centrosymmetric structure. As illustrated in Figure 1c inset, the Cu, In, and P-P pair form triangular patterns within a CIPS layer. Also note that the displaced Cu and In atoms form hexagonal in-plane polar lattices, suggesting that the inversion symmetry is broken in CIPS, which is considered to be the origin of the SHG from CIPS. The nonlinear effect observed in CIPS makes it a promising candidate for various nonlinear optical applications, such as wavelength conversion, light generation, and modulators.

Next, we investigate the SHG intensity as a function of CIPS layer thickness. Figure 1d shows the optical image of a CIPS flake on fused silica with thicknesses ranging from about 10 to 300 nm. The corresponding SHG imaging (Figure 1e) shows the obvious thickness-dependent optical contrast. Figure 1f displays the dependence of SHG signal on CIPS thickness (d). Below 50 nm ($d < 50$ nm), the SHG intensity increases linearly with thickness ($I_{SHG} \propto d$). This thickness scaling behavior is different from most of other vdW structures (e.g., $AgInP_2S_6$,[39] 2H TMDCs,[27] etc.) but is similar to that of 3R TMDCs,[40] revealing that the stacking order in layered CIPS is along the same direction. Therefore, the total SHG intensity is considered to the sum of contributions from individual CIPS layers, $I_{SHG} = nI_0$, where n and I_0 are the number of layer and the SHG intensity for 1L CIPS, respectively. When d is between 50 nm and 110 nm, the SHG intensity decreases with increasing d, which may be explained by nonlinear optical signal reabsorption as well as reflection of incident light in thick-layer sample.[28, 41] Interestingly, SHG intensity starts to slowly increase again as the CIPS thickness is beyond 110 nm and reaches a maximum as d is close to bulk-like dimension (~300 nm). The likely reason is that a structural phase transition occurs at a critical thickness ($d_c \sim 110$ nm),[42] and

this phase transition may significantly change the intrinsic optical characteristics (e.g., nonlinear absorption coefficient, refractive index, etc.) of ferroelectric CIPS.

To probe the effect of crystal structure symmetry in CIPS, polarization-resolved SHG measurement is performed on the sample with different layer thicknesses (Figure 1g). An excitation laser beam is linearly polarized and focused onto the sample, with the analyzer direction (open yellow arrow) parallel to the incident laser polarization (red solid arrow). The polarized SHG signal is collected in reflection mode by rotating the sample within the *x*-*y* plane from angle $\varphi = 0^{o}$ to 360^{o} in 10^{o} steps. Figures 1h and 1i represent the polarization-resolved SHG from a multilayer (~18 nm) and a thick-layer (~133 nm) CIPS, respectively, in Figure 1g. As expected, the hexagonal symmetry of the shifted Cu and In atoms (Figure 1c inset) leads to a characteristic six-fold petal pattern. In addition, for both samples the two petals lying along $\varphi \approx 83^{o}$ and 263^{o} direction (*b*-axis) show stronger polarization. Here, we define the polarization ratio as I_{max}/I_0, where I_{max} is the maximum enhanced SHG polarization intensity along *b*-axis direction and I_0 is the maximum SHG intensity along a mirror plane. The ratio of I_{max}/I_0 for CIPS in Figure 1h and 1i is the same, which is estimated to be ~1.35. This anisotropic SHG pattern behavior appears in CIPS flakes with various thicknesses (Figure S1), and the polarization ratio is insensitive to the layer thickness.

To understand the angular dependence of SHG and establish a relationship between SHG response and ferroelectricity, we perform an *in situ* PFM study. Figures 1j and 1k show the vertical PFM (V-PFM) amplitude images taken on the CIPS sample with thickness of 18 nm and 133 nm, respectively, in Figure 1g. The CIPS film exhibits isolated and highly-ordered rod-shaped nanodomains with uniform upward polarization (P_{up}) direction.[43-47] In addition, the domains with rod shapes are observed in CIPS flakes with various thicknesses (Figure S2a and S2b), which is different to the previously reported results.[4] At the same time, we have performed lateral PFM (L-PFM) measurement (Figure S2c and S2d). The L-PFM signal on the same domain region is very weak and close to the noise level, further confirming that the nanodomains in CIPS possess out-of-plane polarization. The

long axis of these rod-like domains is always along the *a*-axis of CIPS, and is perpendicular to the maximum enhanced SHG polarization direction (*b*-axis) (Figure 1h-i and Figure S1). Similar highly ordered nanodomains have been reported in other as-grown 2D ferroelectrics, such as monoclinic 2D $KNbO_3$ with low-symmetry phase,[48] which was ascribed to the large lattice strain energy stored in the low-symmetry lattice. Based on these analyses, it is reasonable to assume that the observed rod-like nanodomains ($\perp$ *b*-axis) and the enhanced SHG polarization ($\parallel$ *b*-axis) are probably due to the magnified asymmetric structure in CIPS caused by the naturally forming strain along *a*-axis direction (ε_a). In this scenario, the anisotropic SHG pattern behavior in CIPS can be qualitatively described as follows:[49-50]

$$I_{\mathrm{SHG}} = |\mathrm{A}\cos 3(\varphi + \varphi_{\mathrm{o}}) + \mathrm{B}\cos^3(\varphi + \varphi_{\mathrm{o}}) - \mathrm{C}\sin^3(\varphi + \varphi_{\mathrm{o}})\cos(\varphi + \varphi_{\mathrm{o}})|^2, \quad (1)$$

where A, B, and C are three parameters that are related to tensor elements and/or strain ε_a of CIPS. Here, the first term indicates the symmetry property of CIPS, while the latter two terms reflect the strain effect.

The unusual second-harmonic behaviors observed in CIPS can be exploited to design more complex nonlinear optical responses in CIPS-based heterostructures. In previous studies, CIPS has been integrated with 2D semiconductors to construct electronic devices such as ferroelectric field effect transistors and negative capacitance transistors.[2] While 2D TMDCs also exhibit excellent nonlinear optical properties, the SHG response at the heterointerface between CIPS and TMDC is yet to be explored.

Tunable SHG Response in CIPS/1L-MoS_2 Heterostructures. 1L TMDCs, such as MoS_2, have been shown to exhibit strong SHG response due to broken inversion symmetry,[27, 31] which can be tuned by an interfacial ferroelectric layer.[23, 51] As a case study, we explore the second-harmonic response at CIPS/1L-MoS_2 heterointerface (Figure 2a). Figure 2b shows the optical image of a 40 nm CIPS flake after two 1L MoS_2 with different crystal orientations partially transferred on top, forming CIPS/1L-MoS_2 heterostructures, which are labeled as CIPS/MoS_2(#1) and CIPS/MoS_2(#2),

respectively. Figure 2c shows the corresponding SHG image as in Figure 2b taken in the reflection mode with no analyzer applied. The SHG intensity of individual 1L MoS_2 is stronger than that of CIPS. Moreover, two CIPS/1L-MoS_2 heterostructure regions exhibit the same SHG intensity, which is about one order of magnitude weaker than that from individual 1L MoS_2. To understand this SHG modulation effect, we need to identify the dominant interlayer coupling mechanisms between CIPS and MoS_2, which may include polar symmetry, light absorption, etc.

Previous studies of 1L MoS_2 interfaced with ferroelectric oxide $Pb(Zr,Ti)O_3$ have revealed strong modulation of SHG due to the interfacial polar coupling.[23, 51] From the point of view of polar symmetry, the SHG response from CIPS/1L-MoS_2 heterostructure should be a coherent superposition of the SH fields from individual CIPS and 1L MoS_2 layers, with a phase difference depending on the stacking angle.[52] To probe the possibility of polar symmetry coupling, we first analyze individual CIPS, 1L MoS_2, and CIPS/MoS_2 heterostructure in Figure 2b by polarization-resolved SHG. The incident light polarization is along the *x*-axis. As shown in Figures 2d-f, the polar plots of parallel polarization-resolved SHG for individual CIPS, 1L-MoS_2(#1) and 1L-MoS_2(#2) all exhibit six-petal patterns, confirming the three-fold rotational symmetry in MoS_2 as well as the crystalline orientation of each flake (inset). Also note that the petals for CIPS are along the direction close to that of 1L-MoS_2(#1), but differ about 30° from 1L-MoS_2(#2), which leads to two different stacking angles in the two CIPS/1L-MoS_2 heterostructures. The polarization-resolved SHG taken at each CIPS/MoS_2 heterostructure region (red curves in Figures 2e-f) also shows a six-petal polarization pattern, but with petals lying along the same direction as the corresponding individual 1L MoS_2. This clearly indicates that the SHG response in the heterostructure is insensitive to the stacking angle. Thus, the strong modulation of SHG in CIPS by interfacing with 1L MoS_2 (Figure 2c) cannot be explained by the coupling of polar axes.

To further confirm the SHG signal at CIPS/1L-MoS_2 heterointerface is not determined by the polar coupling between CIPS and MoS_2, we perform *in situ* temperature-dependent SHG imaging (Figure

3a) using the same sample of Figure 2b. Figure 3b shows the temperature dependence of the SHG intensity for 1L MoS_2, CIPS, and CIPS/1L-MoS_2 heterostructure. As expected, 1L MoS_2 is insensitive to the temperature, which keeps stable SHG signal intensity during the entire heating (25 ºC → 90 ºC) and cooling (90 ºC → 25 ºC) process. In contrast, the SHG signal for CIPS is stable below T_C (~47 ºC), gradually decreases as the temperature is raised, and almost vanishes at high temperature (T = 90 ºC). Upon cooling, both SHG signal and V-PFM amplitude (bottom insets) recover to the initial levels, indicating that an reversible structural change (from nocentrosymmetric to centrosymmetric) accompanying the phase transition (from ferroelectric to paraelectric) occurs in CIPS around T_C.[20] Surprisingly, the thermal behavior of SHG at CIPS/1L-MoS_2 heterointerface is similar to that of individual 1L MoS_2, which is independent of temperature. It suggests that, whether CIPS is in ferroelectric or paraelectric phase state, the SHG signal in CIPS/1L-MoS_2 heterostructure can be well controlled. This result provides strong evidence that the tailored SHG signal at the heterointerface is not caused by the polar symmetry coupling. After comparison, we also note that the SHG signal at high temperature disappears in CIPS but still exists in CIPS/1L-MoS_2 heterostructure. It demonstrates that the SH field generated from CIPS/1L-MoS_2 heterostructure mainly originate from 1L MoS_2 rather than ferroelectric (or paraelectric) CIPS, which is consistent with polarization-resolved SHG analysis (Figures 2d-f).

The light absorption mediated interfacial coupling offers another mechanism to tune the optical properties of CIPS/1L-MoS_2 heterostructure. To evaluate this scenario, we first compare the room-temperature PL spectra of 1L MoS_2, CIPS, and CIPS/1L-MoS_2 heterostructure (Figure 4a-c). Figure 4a shows the PL spectrum of 1L MoS_2, which can be fitted using a mixed Gauss-Lorentzian mode with three peaks associated with the negative trions (A^- at 1.85 eV, red line) and neutral excitons (A^o at 1.88 eV, purple line; B at 2.00 eV, green line).[53] As shown in Figure 4b, the CIPS exhibits a broad PL spectrum, with an emission peak (C, blue line) located at about 2.07 eV, consistent with the previous report.[13] Interestingly, after forming CIPS/1L-MoS_2 heterostructure by transfer of 1L MoS_2

on top of CIPS, the PL intensity of 1L MoS_2 is significantly reduced, while no significant change is observed for PL signal of CIPS (Figure 4c). It suggests that the PL response of 1L MoS_2 can be well modulated by CIPS. Furthermore, we perform *in situ* temperature-dependent PL measurements on 1L MoS_2, CIPS, and CIPS/1L-MoS_2 heterostructure (Figure S3). As expected, the thermal behavior of PL emissions for both individual 1L MoS_2 and 1L MoS_2 on CIPS (Figure 4d) is insensitive to the temperature, while the PL signal for both individual CIPS and CIPS in heterostructure gradually decreases as the temperature is increased due to the phase transition (Figure 4e). These observed PL modulation behaviors are very similar to those of SHG modulation. We thus conclude that CIPS-induced light absorption interfacial coupling plays a critical role in both PL and SHG signal control in CIPS/MoS_2 heterostructures. In addition, it has been reported that light absorption related interfacial coupling sensitively depends on the layer distance.[28, 54] We, therefore, design a sandwich structure by inserting a Al_2O_3 thin film (Figure 4d and Figure S4) to investigate the effect of interlayer spacing on PL response of 1L MoS_2 on CIPS. Figure 4e compares the PL spectra of individual 1L MoS_2, 1L MoS_2 on CIPS, and 1L MoS_2 on CIPS/Al_2O_3. The light absorption mediated interfacial coupling is reduced for the CIPS/1L-MoS_2 heterostructure with a ~4.5 nm Al_2O_3 insertion, as indicated by the PL intensity of 1L MoS_2, which is stronger for 1L MoS_2 on CIPS/Al_2O_3 than that directly interfaced with CIPS.

To understand the role of CIPS as the light-absorbing layer for the tailored SHG response, we quantitatively analyze the effect of CIPS layer thickness on the signal intensity of CIPS/1L-MoS_2 heterostructure. Figure 5a-b shows the optical and SHG images of a 1L MoS_2 transferred on top of a CIPS flake with layer thicknesses ranging from about 5 to 40 nm. As shown in Figure 5c (left panel), the SHG intensity of CIPS/1L-MoS_2 heterostructure decreases exponentially with the layer thickness of CIPS, with the signal in the heterostructure approaching the intensity comparable to the signal of 40 nm CIPS. To evaluate the capability of CIPS in SHG modulation, the intensity change is normalized, which is defined as $(I_{MoS_2} - I_{CIPS/MoS_2})/I_{MoS_2}$. As shown in Figure 5c (right panel), the

SHG intensity for 1L MoS_2 has been efficiently modulated by the thick-layer CIPS, with a modulation depth up to 80 %, which suggests that the tailoring effect is related to the bulk state of CIPS. In addition, we have analyzed CIPS thickness-dependent PL peak intensity and intensity difference for CIPS/1L-MoS_2 (Figure S5 and Figure 5d), where a similar tailoring effect is obtained. It is thus reasonable to assume that the thickness-dependent SHG and PL signal modulation is also originated from the light absorption effect *via* CIPS layers. The schematic in Figure 5e illustrates that the generation of SHG from CIPS/1L-MoS_2 heterostructure is a two-stage process: the electric field of SHG light is first generated in 1L MoS_2, and then partially absorbed as it propagates through CIPS layer. The thicker the CIPS, the more SHG signal of 1L MoS_2 is absorbed. In this scenario, CIPS/1L-MoS_2 heterostructure with the same CIPS thickness should exhibit different SHG responses in the reflection (R-SHG) and transmission (T-SHG) modes, namely, $I_{\mathrm{R-SHG}} < I_{\mathrm{T-SHG}}$. To prove this model, we map both the R-SHG and T-SHG responses for the same CIPS/1L-MoS_2 sample shown in Figure 2 using the same imaging condition (Figure S6). As expected, we observe higher SHG intensity from CIPS/1L MoS_2 heterostructure in the transmission mode than that in the reflection mode, yielding strong support to the scenario for the light adsorption mediated interfacial coupling between CIPS and MoS_2.

CONCLUSIONS

In summary, we report the giant and tunable second-harmonic responses in out-of-plane dominated ferroelectric CIPS and CIPS/1L-MoS_2 heterostructures. The CIPS exhibits strong and anisotropic SHG responses ranging from multi-layer to bulk-like thickness. Polarization-resolved SHG together with *in situ* PFM measurements reveal that the local strain along *a*-axis naturally forms in the exfoliated CIPS. Moreover, we have realized the strong modulation of SHG in CIPS by interfacing with monolayer MoS_2. We show that the tailored SHG signal at CIPS/1L-MoS_2 heterointerface is unrelated to the polar symmetry coupling, but is driven by light absorption mediated interfacial coupling, as firmly evidenced by a combination of polarization, temperature, and thickness-

dependent SHG and PL analyses. On the other hand, the total SHG signal in CIPS/MoS_2 heterostructure is reduced. In the near future, we will interface CIPS with other vdW semiconductors, searching for the material combination that can achieve both enhanced SHG signal and high tunability. Our study not only enhances the understanding of the nonlinear optical properties of 2D ferroelectrics, but also provides a strategy for implementing vdW ferroelectric heterostructure in nanoscale nonlinear optical modulator, optical information storage, and nonlinear optical imaging.

METHODS

Preparation of CIPS Samples and CIPS/1L-MoS_2 Heterostructures. The bulk CIPS and MoS_2 were purchased from HQ Graphene Tech. CIPS flakes with different layer thicknesses were prepared by mechanical exfoliation from their bulk single crystals, and then transferred onto a transparent fused silica substrate. CIPS/1L-MoS_2 heterostructures were prepared by a dry transfer technique.[28, 55] First, 1L MoS_2 flake was exfoliated onto a Gel-film surface, while few- to thick-layer CIPS flake was exfoliated onto a fused silica substrate. Second, 1L MoS_2 flake on Gel-film was aligned with the CIPS on fused silica under an optical microscopy, and then transferred on top of CIPS, forming CIPS/1L-MoS_2 heterostructures. The layer thicknesses of CIPS and MoS_2 flakes were determined by a combined AFM, optical microscopy, and Raman spectroscopy.

SHG Measurements. SHG measurements were carried out in the homemade nonlinear optical microscopy system. Briefly, a linearly polarized Ti:Sapphire femtosecond laser beam (wavelength: 800 nm, duration: 100 fs, repetition rate: 80 MHz) passed a polarizer and was then focused onto the sample surfaces with normal incidence using a water-immersed objective lens. The SHG signals were collected in reflection geometry by PMT detector. In most cases, the signal was collected with no analyzer inserted. For the polarization-resolved SHG measurements, we fixed the incident light and analyzer polarization, and collected the SHG signal by rotating the sample within the *x*-*y* plane from angle $\varphi = 0^{o}$ to 360^{o} in 10^{o} steps. For the temperature-dependent SHG measurements, the sample was

placed on a programmable hot plate, then slowly heated to the target temperature and held for 1 minute before SHG imaging.

Raman and PL Measurements. Raman and PL measurements were performed in a micro-Raman system (Renishaw InVia plus, Renishaw). Raman and PL signal were collected by focusing a 532 nm laser beam onto the sample surfaces through a 50× objective lens.

PFM Measurements. Both vertical and lateral PFM measurements were performed in a Bruker Multimode 8 AFM system with the conductive PtIr-coated tips (SCM-PIT). For PFM imaging, an AC voltage of 0.5 V was applied during scanning.

ASSOCIATED CONTENT

Supporting Information available: The Supporting Information is available free of charge on the ACS Publications website at http://pubs.acs.org.

SHG characterization of a thick-layer ferroelectric CIPS; Vertical and lateral PFM characterization of ferroelectric CIPS; Temperature-dependent PL spectra of 1L MoS_2, CIPS, and CIPS/1L-MoS_2 heterostructure; PL characterization of 1L MoS_2 on Al_2O_3 and SiO_2 substrates; The effect of CIPS layer thickness on PL spectra of CIPS/1L-MoS_2 heterostructure; Reflected and transmitted SHG response of CIPS/1L-MoS_2 heterostructures.

ACKNOWLEDGEMENTS

The work at Dalian University of Technology was supported by the National Natural Science Foundation of China (Grant No. 12274051), the Natural Science Foundation of Liaoning Province (Grant No. 2024-MSBA-06), the Chunhui Project Foundation of the Education Department of China (Grant No. HZKY20220423), and the Fundamental Research Funds for the Central Universities (Grant No. DUT24RC(3)060). The work at University of Nebraska-Lincoln was supported by the U.S. National Science Foundation (NSF) through Grant No. DMR-2118828 and EPSCoR EQUATE Award No. OIA-2044049, and the Nebraska Center for Energy Sciences Research (NCESR).

REFERENCES

(1) Xue, F.; He, J.-H.; Zhang, X., Emerging van der Waals ferroelectrics: Unique properties and novel devices. *Appl. Phys. Rev.* **2021,** *8*, 021316.

(2) Ryu, H.; Xu, K.; Li, D.; Hong, X.; Zhu, W., Empowering 2D nanoelectronics via ferroelectricity. *Appl. Phys. Lett.* **2020,** *117*, 080503.

(3) Qi, L.; Ruan, S.; Zeng, Y.-J., Review on recent developments in 2D ferroelectrics: Theories and applications. *Adv. Mater.* **2021,** *33*, 2005098.

(4) Liu, F.; You, L.; Seyler, K. L.; Li, X.; Yu, P.; Lin, J.; Wang, X.; Zhou, J.; Wang, H.; He, H.; Pantelides, S. T.; Zhou, W.; Sharma, P.; Xu, X.; Ajayan, P. M.; Wang, J.; Liu, Z., Room-temperature ferroelectricity in $CuInP_2S_6$ ultrathin flakes. *Nat. Commun.* **2016,** *7*, 12357.

(5) Chang, K.; Liu, J.; Lin, H.; Wang, N.; Zhao, K.; Zhang, A.; Jin, F.; Zhong, Y.; Hu, X.; Duan, W.; Zhang, Q.; Fu, L.; Xue, Q.-K.; Chen, X.; Ji, S.-H., Discovery of robust in-plane ferroelectricity in atomic-thick SnTe. *Science* **2016,** *353*, 274-278.

(6) Cui, C.; Hu, W.-J.; Yan, X.; Addiego, C.; Gao, W.; Wang, Y.; Wang, Z.; Li, L.; Cheng, Y.; Li, P.; Zhang, X.; Alshareef, H. N.; Wu, T.; Zhu, W.; Pan, X.; Li, L.-J., Intercorrelated in-plane and out-of-plane ferroelectricity in ultrathin two-dimensional layered semiconductor In_2Se_3. *Nano Lett.* **2018,** *18*, 1253-1258.

(7) Belianinov, A.; He, Q.; Dziaugys, A.; Maksymovych, P.; Eliseev, E.; Borisevich, A.; Morozovska, A.; Banys, J.; Vysochanskii, Y.; Kalinin, S. V., $CuInP_2S_6$ room temperature layered ferroelectric. *Nano Lett.* **2015,** *15*, 3808-3814.

(8) Balke, N.; Neumayer, S. M.; Brehm, J. A.; Susner, M. A.; Rodriguez, B. J.; Jesse, S.; Kalinin, S. V.; Pantelides, S. T.; McGuire, M. A.; Maksymovych, P., Locally controlled Cu-Ion transport in layered ferroelectric $CuInP_2S_6$. *ACS Appl. Mater. Interfaces* **2018,** *10*, 27188-27194.

(9) Liubachko, V.; Shvalya, V.; Oleaga, A.; Salazar, A.; Kohutych, A.; Pogodin, A.; Vysochanskii, Y. M., Anisotropic thermal properties and ferroelectric phase transitions in layered $CuInP_2S_6$ and $CuInP_2Se_6$ crystals. *J. Phys. Chem. Solids* **2017,** *111*, 324-327.

(10) You, L.; Zhang, Y.; Zhou, S.; Chaturvedi, A.; Morris, S. A.; Liu, F.; Chang, L.; Ichinose, D.; Funakubo, H.; Hu, W.; Wu, T.; Liu, Z.; Dong, S.; Wang, J., Origin of giant negative piezoelectricity in a layered van der Waals ferroelectric. *Sci. Adv.* **2019,** *5*, eaav3780.

(11) Neumayer, S. M.; Eliseev, E. A.; Susner, M. A.; Tselev, A.; Rodriguez, B. J.; Brehm, J. A.; Pantelides, S. T.; Panchapakesan, G.; Jesse, S.; Kalinin, S. V.; McGuire, M. A.; Morozovska, A. N.; Maksymovych, P.; Balke, N., Giant negative electrostriction and dielectric tunability in a van der Waals layered ferroelectric. *Phys. Rev. Mater.* **2019,** *3*, 024401.

(12) Neumayer, S. M.; Tao, L.; O'Hara, A.; Brehm, J.; Si, M.; Liao, P.-Y.; Feng, T.; Kalinin, S. V.; Ye, P. D.; Pantelides, S. T.; Maksymovych, P.; Balke, N., Alignment of polarization against an electric field in van der Waals ferroelectrics. *Phys. Rev. Appl.* **2020,** *13*, 064063.

(13) Kong, F.; Zhang, L.; Cong, T.; Wu, Z.; Liu, K.; Sun, C.; Pan, L.; Li, D., Tunable photochemical deposition of silver nanostructures on layered ferroelectric $CuInP_2S_6$. *J. Appl. Phys.* **2022,** *132*, 044103.

(14) Si, M.; Liao, P.-Y.; Qiu, G.; Duan, Y.; Ye, P. D., Ferroelectric field-effect transistors based on MoS_2 and $CuInP_2S_6$ two-dimensional van der Waals heterostructure. *ACS Nano* **2018,** *12*, 6700-6705.

(15) Singh, P.; Baek, S.; Yoo, H. H.; Niu, J.; Park, J.-H.; Lee, S., Two-dimensional CIPS-InSe van der Waal heterostructure ferroelectric field effect transistor for nonvolatile memory applications. *ACS Nano* **2022,** *16*, 5418-5426.

(16) Dey, A.; Yan, W.; Balakrishnan, N.; Xie, S.; Kudrynskyi, Z. R.; Makarovskiy, O.; Yan, F.; Wang, K.; Patanè, A., Memristive effects due to charge transfer in graphene gated through ferroelectric $CuInP_2S_6$. *2D Mater.* **2022,** *9*, 035003.

(17) Wang, X.; Yu, P.; Lei, Z.; Zhu, C.; Cao, X.; Liu, F.; You, L.; Zeng, Q.; Deng, Y.; Zhu, C.; Zhou, J.; Fu, Q.; Wang, J.; Huang, Y.; Liu, Z., Van der Waals negative capacitance transistors. *Nat. Commun.* **2019,** *10*, 3037.

(18) Zhao, Z.; Xu, K.; Ryu, H.; Zhu, W., Strong temperature effect on the ferroelectric properties of $CuInP_2S_6$ and its heterostructures. *ACS Appl. Mater. Interfaces* **2020,** *12*, 51820-51826.

(19) Wu, J.; Chen, H.-Y.; Yang, N.; Cao, J.; Yan, X.; Liu, F.; Sun, Q.; Ling, X.; Guo, J.; Wang, H., High tunnelling electroresistance in a ferroelectric van der Waals heterojunction via giant barrier height modulation. *Nat. Electron.* **2020,** *3*, 466-472.

(20) Misuryaev, T. V.; Murzina, T. V.; Aktsipetrov, O. A.; Sherstyuk, N. E.; Cajipe, V. B.; Bourdon, X., Second harmonic generation in the lamellar ferrielectric $CuInP_2S_6$. *Solid State Commun.* **2000,** *115*, 605-608.

(21) Li, Y.; Fu, J.; Mao, X.; Chen, C.; Liu, H.; Gong, M.; Zeng, H., Enhanced bulk photovoltaic effect in two-dimensional ferroelectric $CuInP_2S_6$. *Nat. Commun.* **2021,** *12*, 5896.

(22) Ma, Y.; Yi, H.; Liang, H.; Wang, W.; Zheng, Z.; Yao, J.; Yang, G., Low-dimensional van der Waals materials for linear-polarization-sensitive photodetection: materials, polarizing strategies and applications. *Mater. Futures* **2024,** *3*, 012301.

(23) Li, D.; Huang, X.; Xiao, Z.; Chen, H.; Zhang, L.; Hao, Y.; Song, J.; Shao, D.-F.; Tsymbal, E. Y.; Lu, Y.; Hong, X., Polar coupling enabled nonlinear optical filtering at MoS_2/ferroelectric heterointerfaces. *Nat. Commun.* **2020,** *11*, 1422.

(24) Guo, Q.; Qi, X.-Z.; Zhang, L.; Gao, M.; Hu, S.; Zhou, W.; Zang, W.; Zhao, X.; Wang, J.; Yan, B.; Xu, M.; Wu, Y.-K.; Eda, G.; Xiao, Z.; Yang, S. A.; Gou, H.; Feng, Y. P.; Guo, G.-C.; Zhou, W.; Ren, X.-F.; Qiu, C.-W.; Pennycook, S. J.; Wee, A. T. S., Ultrathin quantum light source with van der Waals $NbOCl_2$ crystal. *Nature* **2023,** *613*, 53-59.

(25) Guo, Q.; Zhang, Q.; Zhang, T.; Zhou, J.; Xiao, S.; Wang, S.; Feng, Y. P.; Qiu, C.-W., Colossal in-plane optical anisotropy in a two-dimensional van der Waals crystal. *Nat. Photonics* **2024**, 1-6.

(26) Yang, H.; Jussila, H.; Autere, A.; Komsa, H.-P.; Ye, G.; Chen, X.; Hasan, T.; Sun, Z., Optical waveplates based on birefringence of anisotropic two-dimensional layered materials. *ACS Photonics* **2017,** *4*, 3023-3030.

(27) Li, Y.; Rao, Y.; Mak, K. F.; You, Y.; Wang, S.; Dean, C. R.; Heinz, T. F., Probing symmetry properties of few-layer MoS_2 and h-BN by optical second-harmonic generation. *Nano Lett.* **2013,** *13*, 3329-3333.

(28) Li, D.; Xiong, W.; Jiang, L.; Xiao, Z.; Rabiee Golgir, H.; Wang, M.; Huang, X.; Zhou, Y.; Lin, Z.; Song, J.; Ducharme, S.; Jiang, L.; Silvain, J.-F.; Lu, Y., Multimodal nonlinear optical imaging of MoS_2 and MoS_2-based van der Waals heterostructures. *ACS Nano* **2016,** *10*, 3766-3775.

(29) Le, C. T.; Clark, D. J.; Ullah, F.; Senthilkumar, V.; Jang, J. I.; Sim, Y.; Seong, M.-J.; Chung, K.-H.; Park, H.; Kim, Y. S., Nonlinear optical characteristics of monolayer $MoSe_2$. *Ann. Phys.* **2016,** *528*, 551-559.

(30) Zhou, X.; Cheng, J.; Zhou, Y.; Cao, T.; Hong, H.; Liao, Z.; Wu, S.; Peng, H.; Liu, K.; Yu, D., Strong second-harmonic generation in atomic layered GaSe. *J. Am. Chem. Soc.* **2015,** *137*, 7994-7997.

(31) Malard, L. M.; Alencar, T. V.; Barboza, A. P. M.; Mak, K. F.; de Paula, A. M., Observation of intense second harmonic generation from MoS_2 atomic crystals. *Phys. Rev. B* **2013,** *87*, 201401.

(32) Abdelwahab, I.; Tilmann, B.; Wu, Y.; Giovanni, D.; Verzhbitskiy, I.; Zhu, M.; Berté, R.; Xuan, F.; Menezes, L. d. S.; Eda, G.; Sum, T. C.; Quek, S. Y.; Maier, S. A.; Loh, K. P., Giant second-harmonic generation in ferroelectric $NbOI_2$. *Nat. Photonics* **2022,** *16*, 644-650.

(33) Xiao, J.; Zhu, H.; Wang, Y.; Feng, W.; Hu, Y.; Dasgupta, A.; Han, Y.; Wang, Y.; Muller, D. A.; Martin, L. W.; Hu, P.; Zhang, X., Intrinsic two-dimensional ferroelectricity with dipole locking. *Phys. Rev. Lett.* **2018,** *120*, 227601.

(34) Bu, K.; Fu, T.; Du, Z.; Feng, X.; Wang, D.; Li, Z.; Guo, S.; Sun, Z.; Luo, H.; Liu, G.; Ding, Y.; Zhai, T.; Li, Q.; Lü, X., Enhanced second-harmonic generation of van der Waals $CuInP_2S_6$ via pressure-regulated cationic displacement. *Chem. Mater.* **2023,** *35*, 242-250.

(35) Rahman, S.; Yildirim, T.; Tebyetekerwa, M.; Khan, A. R.; Lu, Y., Extraordinary nonlinear optical interaction from strained nanostructures in van der Waals $CuInP_2S_6$. *ACS Nano* **2022,** *16*, 13959-13968.

(36) Maisonneuve, V.; Evain, M.; Payen, C.; Cajipe, V. B.; Molinié, P., Room-temperature crystal structure of the layered phase $Cu_{I}In_{III}P_2S_6$. *J. Alloy. Compd.* **1995,** *218*, 157-164.

(37) Vysochanskii, Y. M.; Stephanovich, V. A.; Molnar, A. A.; Cajipe, V. B.; Bourdon, X., Raman spectroscopy study of the ferrielectric-paraelectric transition in layered $CuInP_2S_6$. *Phys. Rev. B* **1998,** *58*, 9119-9124.

(38) Zhou, S.; You, L.; Zhou, H.; Pu, Y.; Gui, Z.; Wang, J., Van der Waals layered ferroelectric $CuInP_2S_6$: Physical properties and device applications. *Front. Phys.* **2020,** *16*, 13301.

(39) Wang, X.; Du, K.; Liu, W.; Hu, P.; Lu, X.; Xu, W.; Kloc, C.; Xiong, Q., Second-harmonic generation in quaternary atomically thin layered $AgInP_2S_6$ crystals. *Appl. Phys. Lett.* **2016,** *109*, 123103.

(40) Shi, J.; Yu, P.; Liu, F.; He, P.; Wang, R.; Qin, L.; Zhou, J.; Li, X.; Zhou, J.; Sui, X.; Zhang, S.; Zhang, Y.; Zhang, Q.; Sum, T. C.; Qiu, X.; Liu, Z.; Liu, X., 3R MoS_2 with broken inversion symmetry: A promising ultrathin nonlinear optical device. *Adv. Mater.* **2017,** *29*, 1701486.

(41) Hendry, E.; Hale, P. J.; Moger, J.; Savchenko, A. K.; Mikhailov, S. A., Coherent nonlinear optical response of graphene. *Phys. Rev. Lett.* **2010,** *105*, 097401.

(42) Deng, J.; Liu, Y.; Li, M.; Xu, S.; Lun, Y.; Lv, P.; Xia, T.; Gao, P.; Wang, X.; Hong, J., Thickness-dependent in-plane polarization and structural phase transition in van der Waals ferroelectric $CuInP_2S_6$. *Small* **2020,** *16*, 1904529.

(43) Ming, W.; Huang, B.; Zheng, S.; Bai, Y.; Wang, J.; Wang, J.; Li, J., Flexoelectric engineering of van der Waals ferroelectric $CuInP_2S_6$. *Sci. Adv.* **2022,** *8*, eabq1232.

(44) Xu, D.-D.; Ma, R.-R.; Zhao, Y.-F.; Guan, Z.; Zhong, Q.-L.; Huang, R.; Xiang, P.-H.; Zhong, N.; Duan, C.-G., Unconventional out-of-plane domain inversion via in-plane ionic migration in a van der Waals ferroelectric. *J. Mater. Chem. C* **2020,** *8*, 6966-6971.

(45) Susner, M. A.; Chyasnavichyus, M.; Puretzky, A. A.; He, Q.; Conner, B. S.; Ren, Y.; Cullen, D. A.; Ganesh, P.; Shin, D.; Demir, H.; McMurray, J. W.; Borisevich, A. Y.; Maksymovych, P.; McGuire, M. A., Cation–eutectic transition via sublattice melting in $CuInP_2S_6/In_{4/3}P_2S_6$ van der Waals layered crystals. *ACS Nano* **2017,** *11*, 7060-7073.

(46) Chyasnavichyus, M.; Susner, M. A.; Ievlev, A. V.; Eliseev, E. A.; Kalinin, S. V.; Balke, N.; Morozovska, A. N.; McGuire, M. A.; Maksymovych, P., Size-effect in layered ferrielectric $CuInP_2S_6$. *Appl. Phys. Lett.* **2016,** *109*, 172901.

(47) Wang, K.; Li, D.; Wang, J.; Hao, Y.; Anderson, H.; Yang, L.; Hong, X., Interface-tuning of ferroelectricity and quadruple-well state in $CuInP_2S_6$ via ferroelectric oxide. *ACS Nano* **2023,** *17*, 15787-15795.

(48) Zhou, F.; Li, Y.; Liao, X.; Lin, S.; Song, H.; Liu, Y.; Yang, F.; Yan, S.; Lai, Z.; Liu, Y.; Xu, C.-Y.; Yang, Z.; Huang, Y.; Zhen, L.; Zhu, J.; Yao, J., Topotactic growth of free-standing two-dimensional perovskite niobates with low symmetry phase. *Nano Lett.* **2021,** *21*, 4700-4707.

(49) Liang, J.; Zhang, J.; Li, Z.; Hong, H.; Wang, J.; Zhang, Z.; Zhou, X.; Qiao, R.; Xu, J.; Gao, P.; Liu, Z.; Liu, Z.; Sun, Z.; Meng, S.; Liu, K.; Yu, D., Monitoring local strain vector in atomic-layered $MoSe_2$ by second-harmonic generation. *Nano Lett.* **2017,** *17*, 7539-7543.

(50) Li, D.; Wei, C.; Song, J.; Huang, X.; Wang, F.; Liu, K.; Xiong, W.; Hong, X.; Cui, B.; Feng, A.; Jiang, L.; Lu, Y., Anisotropic enhancement of second-harmonic generation in monolayer and bilayer MoS_2 by integrating with TiO_2 nanowires. *Nano Lett.* **2019,** *19*, 4195-4204.

(51) Li, D.; Huang, X.; Wu, Q.; Zhang, L.; Lu, Y.; Hong, X., Ferroelectric domain control of nonlinear light polarization in MoS_2 via $PbZr_{0.2}Ti_{0.8}O_3$ thin films and free-standing membranes. *Adv. Mater.* **2023,** *35*, 2208825.

(52) Hsu, W.-T.; Zhao, Z.-A.; Li, L.-J.; Chen, C.-H.; Chiu, M.-H.; Chang, P.-S.; Chou, Y.-C.; Chang, W.-H., Second harmonic generation from artificially stacked transition metal dichalcogenide twisted bilayers. *ACS Nano* **2014,** *8*, 2951-2958.

(53) Li, D.; Xiao, Z.; Golgir, H. R.; Jiang, L.; Singh, V. R.; Keramatnejad, K.; Smith, K. E.; Hong, X.; Jiang, L.; Silvain, J. F., Large-area 2D/3D MoS_2–MoO_2 heterostructures with thermally stable exciton and intriguing electrical transport behaviors. *Adv. Electron. Mater.* **2017,** *3*, 1600335.

(54) Fang, H.; Battaglia, C.; Carraro, C.; Nemsak, S.; Ozdol, B.; Kang, J. S.; Bechtel, H. A.; Desai, S. B.; Kronast, F.; Unal, A. A.; Conti, G.; Conlon, C.; Palsson, G. K.; Martin, M. C.; Minor, A. M.; Fadley, C. S.; Yablonovitch, E.; Maboudian, R.; Javey, A., Strong interlayer coupling in van der Waals heterostructures built from single-layer chalcogenides. *P. Natl. Acad. Sci.* **2014,** *111*, 6198-6202.

(55) Castellanos-Gomez, A.; Buscema, M.; Molenaar, R.; Singh, V.; Janssen, L.; van der Zant, H. S. J.; Steele, G. A., Deterministic transfer of two-dimensional materials by all-dry viscoelastic stamping. *2D Mater.* **2014,** *1*, 011002.

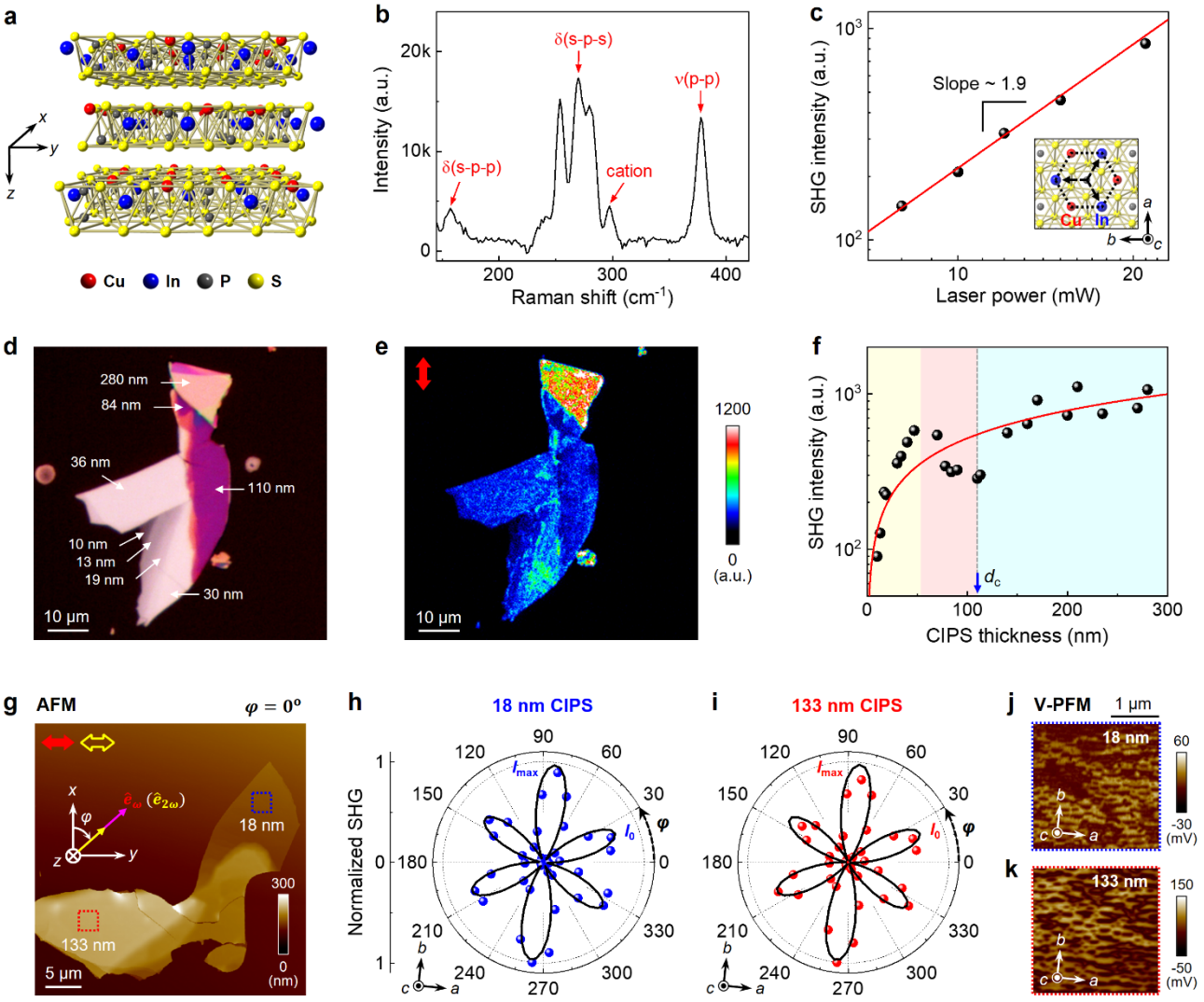

Figure 1. Observation of anisotropic SHG in ferroelectric CIPS. (a) Schematic of atomic structure for CIPS. (b) Raman spectrum for a thick CIPS layer. (c) Excitation laser power dependence of the SHG intensity from a thick-layer CIPS. The solid line is fitted with a slope of 1.9 ± 0.2. Inset: top view of the CIPS crystal structure. (d) Optical image of an exfoliated CIPS flake with different layer thicknesses on fused silica substrate. (e) SHG mapping of the same CIPS sample in (d). The red arrow indicates the incident light polarization. (f) SHG signal as a function of CIPS layer thickness. (g) AFM image of an exfoliated CIPS flake with two different layer thicknesses. The laboratory coordinate system is shown as inset. (h-i) Polar plots of parallel polarized SHG intensity for (h) 18 nm and (i) 133 nm thick CIPS in (g) as a function of the sample rotation angle φ. The dots are experimental data with fits in solid lines. The red solid (yellow open) arrows in (g) mark the incident light (analyzer) polarization. (j-k) Vertical PFM amplitude images taken on the sample in (g) at blue boxed area (j) and red boxed area (k). The crystalline orientations of CIPS are shown as insets.

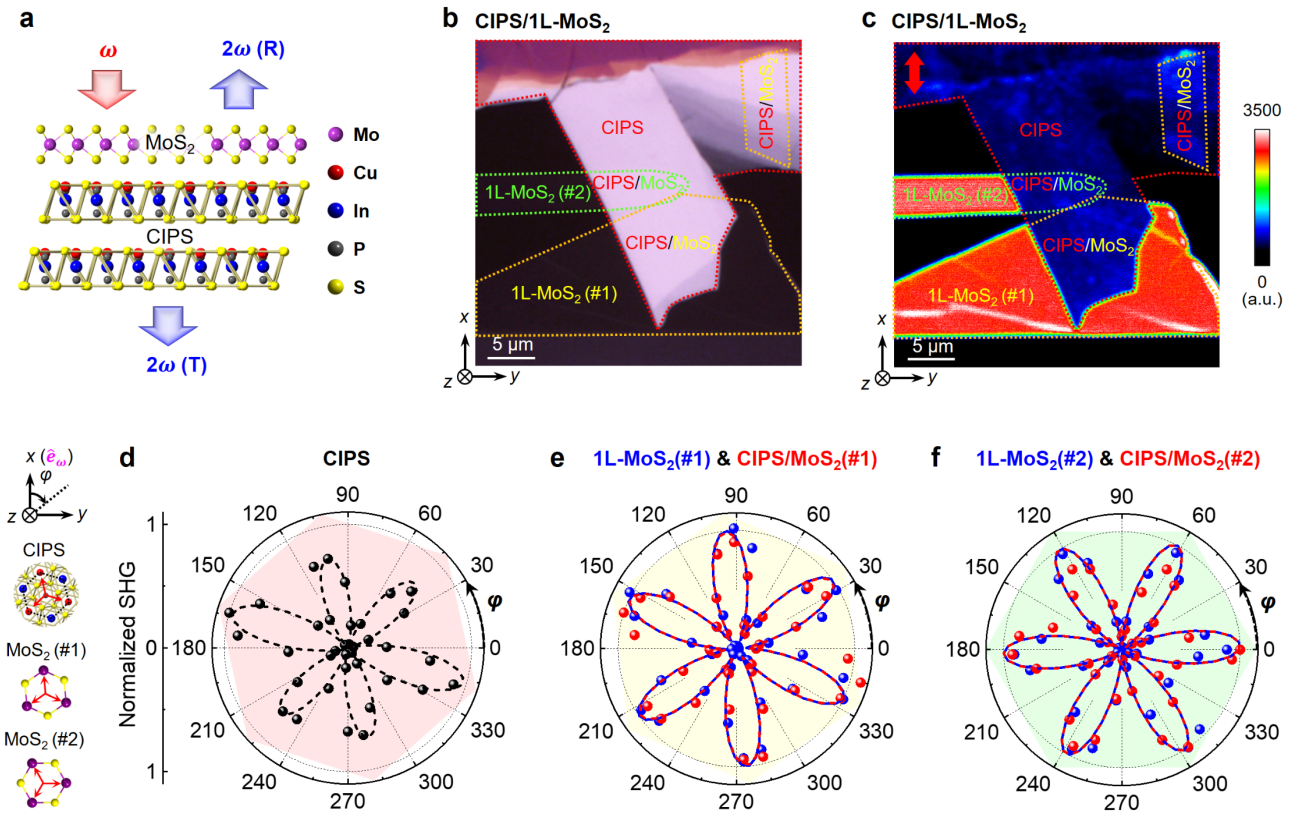

Figure 2. SHG characterization of CIPS/1L-MoS_2 heterostructures. (a) Schematic of CIPS/1L-MoS_2 heterostructure. (b) Optical image and (c) SHG mapping in the reflection mode of a thick-layer CIPS flake after two 1L MoS_2 with different crystal orientations partially transferred on top. The regions of CIPS, 1L-MoS_2(#1), and 1L-MoS_2(#2) are, respectively, labelled with red, yellow, and green dotted lines. The red arrow in (c) indicates the incident light polarization. No analyzer is applied. (d-f) Polar plots of parallel polarized SHG intensity for the sample in (b) as a function of the sample rotation angle φ, taken at regions of (d) CIPS, (e) 1L-MoS_2(#1) and CIPS/MoS_2(#1), and (f) 1L-MoS_2(#2) and CIPS/MoS_2(#2). The dots are experimental data with fits in dashed lines. The laboratory coordinate system, and crystal orientations of CIPS and MoS_2 are shown as left insets.

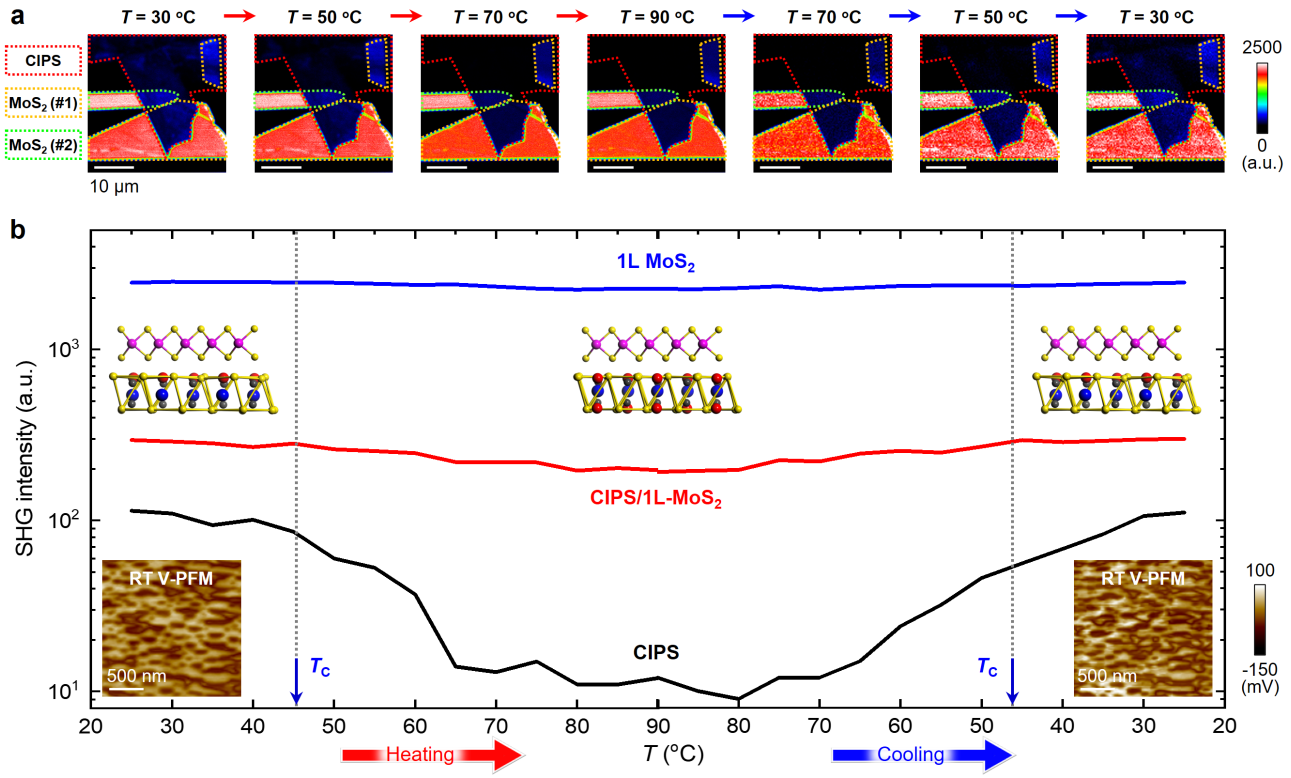

Figure 3. Temperature-dependent SHG response in CIPS/1L-MoS_2 heterostructures. (a) *In situ* temperature-dependent SHG imaging of the CIPS/1L-MoS_2 heterostructure in Fig. 2b. (b) SHG intensity versus *T* curves for 1L MoS_2 (blue), CIPS (black), and CIPS/1L-MoS_2 heterostructure (red). Bottom insets: vertical PFM amplitude images of CIPS taken at room temperature before (left) and after (right) heating treatment.

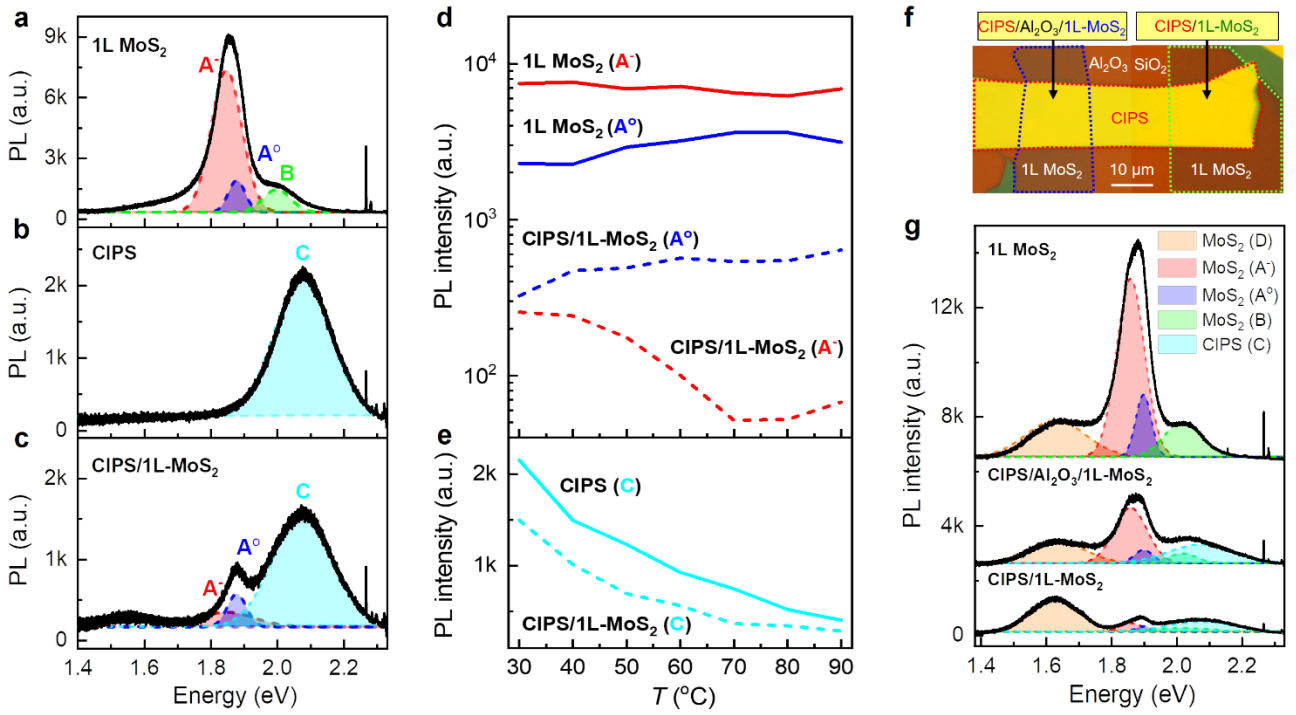

Figure 4. PL characterization of CIPS/1L-MoS_2 heterostructures. (a-c) Room temperature PL spectra of the (a) 1L MoS_2, (b) CIPS, and (c) CIPS/1L-MoS_2 heterostructure. The red, purple, and green dashed lines are A^-, A°, and B excitons originated from 1L MoS_2, while the blue dashed line is C excitation originated from CIPS. (d) Temperature dependence of the excitations A^- and A° extracted from 1L MoS_2 and CIPS/1L-MoS_2 heterostructure. (e) Temperature dependence of the excitation C extracted from CIPS and CIPS/1L-MoS_2 heterostructure. (f) Optical image of CIPS/1L-MoS_2 heterostructure on SiO_2/Si substrate, with (left) and without (right) inserting a ~4.5 nm Al_2O_3 film between CIPS and 1L MoS_2. (g) Room temperature PL spectra of the 1L MoS_2, CIPS/Al_2O_3/1L-MoS_2, and CIPS/1L-MoS_2 in (f).

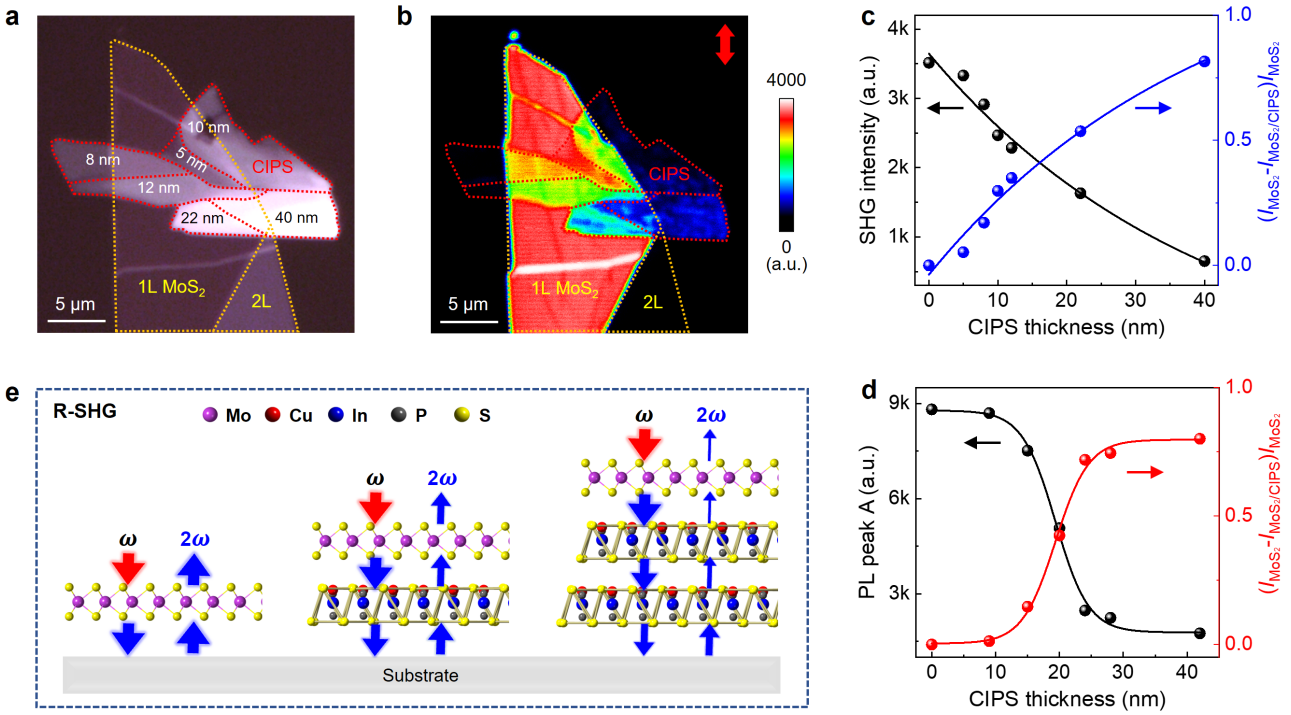

Figure 5. The effect of CIPS layer thickness on SHG response in CIPS/1L-MoS_2 heterostructures. (a) Optical and (b) SHG images of a 1L MoS_2 transferred on top of a CIPS flake with different layer thicknesses. The yellow and red dotted lines mark the MoS_2 and CIPS, respectively. The red arrow in (b) indicates the incident light polarization, and no analyzer is applied. (c) SHG intensity (left) and intensity difference (right) for CIPS/1L-MoS_2 sample in (a) as a function of CIPS layer thickness. (d) PL peak intensity of A excitation (left) and intensity difference (right) for CIPS/1L-MoS_2 sample as a function of CIPS layer thickness. (e) Schematic illustration of SHG process at CIPS/1L-MoS_2 heterointerface in reflection mode.

Table of Contents Graphic